THE JOURNAL OF PHYSICAL CHEMISTRY C

Article

pubs.acs.org/JPCC

Structural, Magnetic, and Thermodynamic Evolutions of Zn-Doped Fe_3O_4 Nanoparticles Synthesized Using a One-Step Solvothermal Method

Xin Liu,[†] Jun Liu,[‡] Shihui Zhang,[†] Zhaodong Nan,*[,‡] and Quan Shi*[,†]

[†]Dalian Institute of Chemical Physics, Chinese Academy of Sciences, Dalian 116023, China

[‡]College of Chemistry and Chemical Engineering, Yang Zhou University, Yangzhou 225002, China

Supporting Information

ABSTRACT: Zn-doped Fe_3O_4 magnetic nanoparticles represented as $Zn_xFe_{3-x}O_4$ with different Zn contents of x varying from 0.0 to 1.0 were synthesized using a facile one-step solvothermal method. The Zn/Fe ratio in these particles could be accurately controlled using this facile synthesis technique. The ICP-OES and XRD measurements indicated that in the x range from 0 to 0.4 the doped Zn^{2+} may replace the Fe^{3+} at the A site and consequently the B-site Fe^{2+} changed to Fe^{3+}, while above 0.4 the Zn^{2+} tends to replace the B-site Fe^{2+}. The morphologies and size distributions of these samples characterized from the TEM showed that the nanoparticles appeared to aggregate into magnetic nanocrystal clusters with varying cluster sizes and different Zn doping contents. The magnetic measurement and Mössbauer spectra investigation revealed that the magnetic properties of the $Zn_xFe_{3-x}O_4$ would exhibit a sensitive dependence with the doped Zn variations. Most importantly, the heat capacity studies illuminated that, at low temperatures, the samples could have a ferromagnetic contribution with x = 0.0 and 0.2 and turn to an antiferromagnetic contribution with x = 0.5, 0.8, and 1.0.

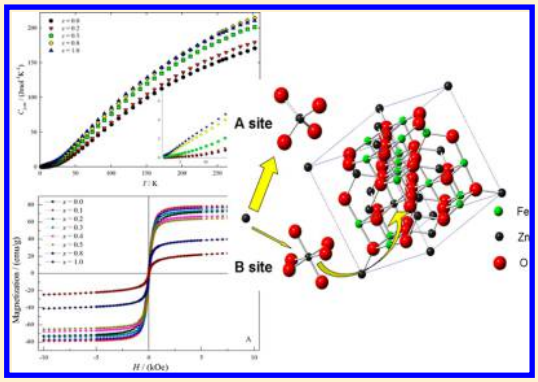

1. INTRODUCTION

In the past decades, magnetic nanoparticles have been an important subject of materials research due to their unique magnetic properties and broad potential applications, including high density data storage,[1] drug delivery,[2] magnetic resonance imaging (MRI) contrast enhancements,[3] bioseparations,[4] biosensors,[5−7] and magnetic hyperthermia.[2,8] Among these materials, Fe_3O_4 nanoparticles have been intensively investigated because of their fantastic electric, highly biocompatible, and remarkable magnetic properties.[9−14] However, Fe_3O_4 nanoparticles usually exhibit a relatively low magnetization value as the particle sizes are located at the nanoscale, which has always been a considerable obstacle for their practical applications. On the other hand, metal element doping has been widely used to modify or improve the nanoparticles' magnetization, and the doped metals (M) are generally Co, Ba, Cu, Mn, Ni, and Zn.[15−18] In this case, the cation distributions at the tetrahedral (A-site) and octahedral (B-site) sites in the Fe_3O_4 spinel structure are usually represented as $[M_{(1-\delta)}^{2+}Fe_{\delta}^{3+}]_A[M_x^{2+}Fe_{(2-\delta)}^{3+}]_BO_4^{2-}$, where δ is the inversion degree defined as the fraction of A-sites occupied by Fe^{3+} ions or the fraction of B-sites occupied by M^{2+} ions. The magnetization of Fe_3O_4 is therefore mainly originated from the superexchange interactions between A- and B-site cations. Using the method of controlling the M doped amounts and inversions could efficiently modify the interactions between the two sites and eventually improve the corresponding magnetic properties in the materials.[19]

Zinc is one of the commonly used metal dopants into Fe_3O_4 due to its nonmagnetic property. Plenty of synthesis techniques have been proposed for preparing Zn-doped Fe_3O_4 nanoparticles, such as coprecipitation method,[20] sol−gel method,[21] electrochemical synthesis,[22] mechanical alloying,[23] reverse micelles,[24] chemical solution deposition,[25] rapid quenching technique,[26] sputtering processing,[27] solvothermal method,[28] and so on. Among these various methods, solvothermal synthesis has been shown to be attractive and effective because of its nice compositional controls, high yields, and easy operation conditions.[29,30] For instance, Li et al. synthesized magnetic MFe_2O_4 (M = Fe, Co) hollow spheres using a simple template free solvothermal method in ethylene glycol solution; however, they did not attempt to apply this method for preparing $Zn_xFe_{3-x}O_4$ nanoparticles.[28] Another method was also proposed for synthesizing $Zn_xFe_{3-x}O_4$ microspheres, but the Zn doping amounts achieved were only up to x = 0.4.[31] Recently, Yang et al. employed a simple solvothermal process for preparing $Zn_xFe_{3-x}O_4$ hollow nanospheres; however, the synthesis of $ZnFe_3O_4$ was not presented.[32] As can be seen

Received: October 29, 2015
Revised: December 22, 2015
Published: December 23, 2015

ACS Publications © 2015 American Chemical Society

DOI: 10.1021/acs.jpcc.5b10618
J. Phys. Chem. C 2016, 120, 1328−1341

Table 1. Reactant Concentrations in the Synthesis and the Average Diameters of $Zn_xFe_{3-x}O_4$ Samples from TEM

	reactants/mmol		av diameter from TEM/nm	
Zn content (x)	$Fe(NO_3)_3{\cdot}9H_2O$	$Zn(NO_3)_2{\cdot}6H_2O$	nanoclusters	nanoparticles
0.0	18.0	0.0	192	22−24
0.1	17.4	0.6	127	22−24
0.2	16.8	1.2	120	14−16
0.3	16.2	1.8	109	13−15
0.4	15.6	2.4	101	12−14
0.5	15.0	3.0	101	11−13
0.8	13.2	4.8	105	11−13

from these established publications, the synthesis of $Zn_xFe_{3-x}O_4$ nanoparticles with controlled Zn doping amounts is still a challenge in this field. In our most recent work, we have developed a facile one-step solvothermal method for synthesizing stoichiometric zinc ferrite nanocrystal clusters using iron and zinc nitrates as metal sources, in which the nitrate ions was used to reduce the Fe^{2+} concentrations or prevent the Fe^{2+} formation through oxidation and reduction reactions in the polyol solutions.[33] In this work, we have developed this novel method for the preparation of $Zn_xFe_{3-x}O_4$ nanoparticles.

Another aspect of $Zn_xFe_{3-x}O_4$ research is magnetic property studies using a variety of techniques, including magnetic measurements, X-ray diffraction detections, Mössbauer spectra, XPS, neutron diffractions, calorimetric measurements, as well as density functional methods.[34−48] However, it has been generally believed that the magnetic properties of $Zn_xFe_{3-x}O_4$ nanoparticles could be considerably variable with different synthesis methods.[34,48] For example, Liu et al. synthesized a series of Zn-doped Fe_3O_4 nanoparticles using a chemical coprecipitated technique, indicating that a maximum saturation magnetization of 80.93 emu/g could be achieved at x = 0.2; they also found that the x value of 0.4 was likely the zinc doping limit of forming a Zn-doped Fe_3O_4 crystal structure.[34] However, $Zn_xFe_{3-x}O_4$ nanoparticles obtained from a sol−gel approach were reported to exhibit a maximum magnetization of 59 emu/g for x = 0.18 at room temperature and 86 emu/g for x = 0.45 at 5 K.[35] Moreover, the maximum saturation magnetization was reported to be 74.50 emu/g at x = 0.075 from a coprecipitation method developed by Marand et al.,[36] while another work using a hydrothermal method presented that the saturation magnetization increased with zinc contents increasing from 0 to 0.33 and then decreased with further doping Zn in the materails.[37] It should be pointed out that Cheng et al. studied the magnetic properties of $Zn_xFe_{3-x}O_4$ with different Zn doping amounts using a density functional method with generalized-gradient approximation corrected for on-site Coulombic interactions, and the calculation results revealed that the saturation magnetization increased evidently with increasing x from 0 to 0.75 and then decreased rapidly to zero at x = 1.[38]

On the basis of these established works in literature, the magnetic evolution in $Zn_xFe_{3-x}O_4$ nanoparticles in terms of various Zn doping amounts may not be clearly illuminated, and therefore we should pursue other strategies to further cast light upon this interesting topic. It is well-known that heat capacity is a bulk fundamental thermodynamic property of materials, and heat capacity measurement has been proven to be a very powerful technique to investigate and understand lattice vibrations, metals, superconductivities, electronic, and nuclear magnetisms, dilute magnetic systems, structural transitions, heavy Fermions, and so on.[49,50] As for magnetic materials, heat capacity can provide important information about magnetic interactions as well as lattice vibrations associated with crystal structure changes. Rather surprisingly, however, heat capacity investigations on Zn-doped Fe_3O_4 were mainly focused on the Verway transition properties or basic thermodynamic data determinations.[46,47] To our knowledge, systematically low temperature heat capacity studies on the magnetic properties of $Zn_xFe_{3-x}O_4$ nanoparticles with various Zn doping amounts have not been reported until now.

In the present study, we have successfully synthesized a series of $Zn_xFe_{3-x}O_4$ nanoparticles with controlled Zn doping amounts using a novel solvothermal method developed in our previous work.[33] The crystal structures and morphologies have been intensively studied using the ICP, XRD, and TEM techniques. The magnetic and Mössbauer spectra measurements have shown that the Zn doping amounts and inversions could play a crucial role in tuning the magnetic interactions among these nanoparticles. Most importantly, the heat capacity measurements have been systematically performed to investigate the thermodynamic properties of these nanoparticles for the first time. The results indicated that the magnetic heat capacity contributions at low temperatures would change from ferromagnetic to antiferromagnetic with Zn doping amounts increasing from 0 to 1.

2. EXPERIMENTAL SECTION

2.1. Synthesis. All the chemicals were analytical grade regents purchased from Sinopharm Chemical Reagent Company and used without further purification in the synthesis process. The Zn-doped Fe_3O_4 samples were synthesized using a facile one-step solvothermal method developed in our previous work.[33] In general, the starting materials of $Zn(NO_3)_2{\cdot}6H_2O$ and $Fe(NO_3)_3{\cdot}9H_2O$, with different molar amounts listed in Table 1, were dissolved in 50 mL of anhydrous ethylene glycol, and 18.0 mmol of CH_3COONa was consequently added into the mixture. The whole mixture was vigorously stirred for about 5 min to make a homogeneous solution. The solution was then transferred into a 50 mL Teflon-lined stainless steel autoclave, which was thermally treated for 24 h at 200 °C and then naturally cooled to room temperature. This synthesis process yielded a black precipitate. The final product was obtained by washing the precipitate a few times with distilled water and ethanol before being dried in a vacuum oven at 50 °C for 24 h. The synthesized Zn-doped Fe_3O_4 samples were represented as $Zn_xFe_{3-x}O_4$ with (x = 0, 0.1, 0.2, 0.3, 0.4, 0.5, and 0.8) according to the Zn/Fe molar ratios used in the synthesis process. The $Zn_xFe_{3-x}O_4$ sample with (x = 1.0) synthesized and characterized from our previous work[33] was used in the following magnetic, Mössbauer spectra, and heat capacity studies.

2.2. Characterization. The Zn and Fe contents in the $Zn_xFe_{3-x}O_4$ samples were determined using the inductively

DOI: 10.1021/acs.jpcc.5b10618
J. Phys. Chem. C 2016, 120, 1328−1341

coupled plasma atomic emission spectroscopy (ICP-AES) performed on a PerkinElmer ICP-OES Optima 7300 DV system. X-ray powder diffraction (XRD) analysis was conducted using a Bruker D8 Advance X-ray diffractometer with Cu Kα radiation (λ = 1.5418 Å), and scanned over a 2θ range from 10° to 80° in the Bragg configuration. Transmission electron microscopy (TEM) measurements were performed using a Philips Tecnai-12 TEM with an acceleration voltage of 120 kV, in which the $Zn_xFe_{3-x}O_4$ samples were prepared by first being dispersed in absolute ethanol which was followed by placing a drop of that solution onto a lacey copper grid. The dc-magnetic susceptibility was measured using the vibrating sample magnetometry option of a Quantum Design physical property measurement system (PPMS) in the temperature range from 4 to 300 K. Magnetization isotherms were collected at 300 K in the magnetic field from −1 to +1 T. Mössbauer spectra measurements were performed using a conventional acceleration spectrometer in the transmission geometry with a ^{57}Co source in a Rh matrix at 300 K. The parameters of the hyperfine structure of the spectra were determined by fitting the experimental data to the modeled spectrum in a linear approximation based on the least-squares method. Isomer shifts were given relative to the centroid of the calibration spectrum of the α-iron foil at room temperature.

The heat capacities of the $Zn_xFe_{3-x}O_4$ samples were measured using the PPMS in the temperature range from 1.9 to 300 K. The temperature intervals in the measurement were set to be logarithmic and 10 K spacing in the region from 1.9 to 100 K and from 100 to 300 K, respectively. The heat capacity measurement accuracy was verified, by measuring standard materials of α-Al_2O_3, copper pellet, and benzoic acid, to be within ±3% in the temperature range from 1.9 to 20 K and ±1% in the range from 20 to 400 K.[51] The powdered $Zn_xFe_{3-x}O_4$ samples were prepared using a technique of powdered sample PPMS measurements developed by Shi et al., and the detailed sample measurement procedure can be found in the recent publications.[49,52] In general, the powdered sample was mixed with a number of copper stripes within a copper cup, and consequently, the sample, copper stripes, and copper cup were compressed together into a pellet using a stainless steel die. The pellet including the sample and copper was measured on the PPMS, and thus the sample heat capacity can be obtained by subtracting the known heat capacity of copper from the total of the pellet.

3. RESULTS AND DISCUSSION

3.1. ICP, XRD, and TEM Analysis. The Zn and Fe contents in the $Zn_xFe_{3-x}O_4$ samples were determined using the ICP-AES technique, and the results represented as a molar ratio of Zn to Fe (R_{ICP}) as well as the ratio in the starting materials of the synthesis process (R_{syn}) are shown in Figure 1. It can be seen from the figure that R_{ICP} is in good agreement with R_{syn}, indicating that the Zn contents in the $Zn_xFe_{3-x}O_4$ samples could be accurately controlled using our one-step solvothermal synthesis method. The phase structures of the $Zn_xFe_{3-x}O_4$ samples with x from 0.0 to 0.8 were investigated using the XRD instrument, and the collected diffraction patterns are shown in Figure 2. All the reflections could be indexed in the $Fd\bar{3}m$ (No. 227) space group of an ideal cubic structure, suggesting that the samples have a spinel ferrite structure (ICDD No. 22-1012). The lattice parameter (a) and average crystal size calculated from the XRD patterns are listed in Table 2. It can be seen that, with the doped Zn contents increasing

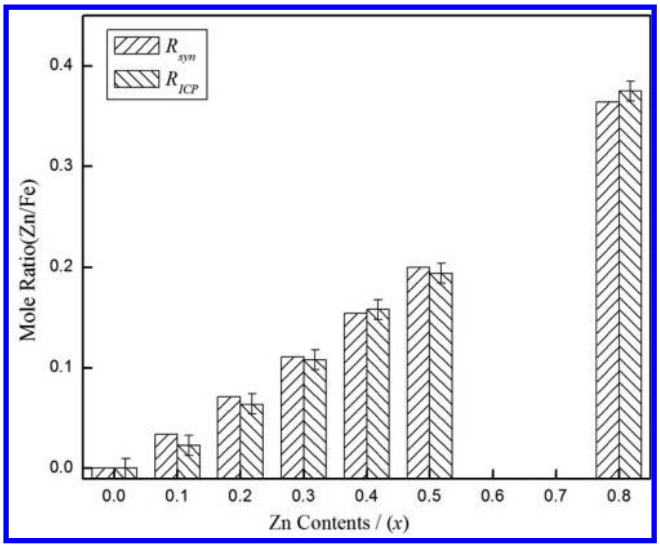

Figure 1. Comparison of Zn/Fe molar ratios in $Zn_xFe_{3-x}O_4$ samples from ICP (R_{ICP}) with those in the synthesis (R_{syn}).

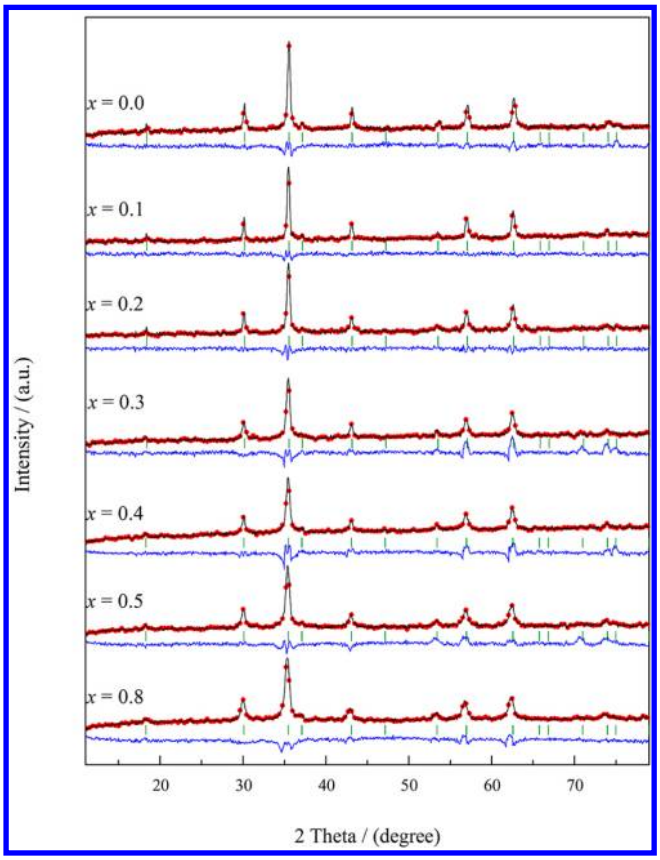

Figure 2. Representative final Rietveld refinements for $Zn_xFe_{3-x}O_4$ samples, showing the comparison of the observed (●) with the calculated (—).

from 0 to 0.8, the lattice parameter tends to increase while the crystal size declines. This observation could be understood from the fact that the radius of Zn^{2+} (74 pm) is larger than those of Fe^{2+} (61 pm) and Fe^{3+} (49 pm), which may induce an increase of the lattice parameter, and consequently, the crystallite size changes with x increasing.[53,54] It is worth noting that Liu et al. also reported a similar effect of x on the length of the a-axis and the crystal size with the Zn contents below 0.4,

DOI: 10.1021/acs.jpcc.5b10618
J. Phys. Chem. C 2016, 120, 1328−1341

Table 2. XRD Results for Lattice Parameter, Crystallite Size, and Rietveld Refinement for $Zn_xFe_{3-x}O_4$ Samples

Zn content (x)	lattice param (Å)	cryst size (nm^3)	composition at A and B sites	χ^2	wR_p/%	R_p/%
0.0	8.3893	27	$(Fe^{3+})_A[Fe^{2+}Fe^{3+}]_BO_4$	0.671	2.35	1.94
0.1	8.3988	27	$(Zn_{0.1}{}^{2+}Fe_{0.9}{}^{3+})_A[Fe_{0.9}{}^{2+}Fe_{1.1}{}^{3+}]_BO_4$	0.410	1.82	1.54
0.2	8.4032	24	$(Zn_{0.2}{}^{2+}Fe_{0.8}{}^{3+})_A[Fe_{0.8}{}^{2+}Fe_{1.2}{}^{3+}]_BO_4$	0.481	4.21	2.22
0.3	8.4097	20	$(Zn_{0.3}{}^{2+}Fe_{0.7}{}^{3+})_A[Fe_{0.7}{}^{2+}Fe_{1.3}{}^{3+}]_BO_4$	1.606	5.89	3.77
0.4	8.4249	17	$(Zn_{0.4}{}^{2+}Fe_{0.6}{}^{3+})_A[Fe_{0.6}{}^{2+}Fe_{1.4}{}^{3+}]_BO_4$	1.370	5.32	3.61
0.5	8.4258	16	$(Zn_{0.4}{}^{2+}Fe_{0.6}{}^{3+})_A[Zn_{0.1}{}^{2+}Fe_{0.5}{}^{2+}Fe_{1.4}{}^{3+}]_BO_4$	1.062	3.95	2.69
0.8	8.427	14	$(Zn_{0.4}{}^{2+}Fe_{0.6}{}^{3+})_A[Zn_{0.4}{}^{2+}Fe_{0.2}{}^{2+}Fe_{1.4}{}^{3+}]_BO_4$	1.357	4.31	3.43

and indicated that the x value of 0.4 might be thought to be an acceptable limit on forming the $Zn_xFe_{3-x}O_4$ crystal.[34] However, in the present study, this interesting x effect on the crystal structure can be well-maintained until x = 0.8, suggesting that the Zn in all of samples can be successfully doped into the Fe_3O_4 lattice.

The XRD refinement of the $Zn_xFe_{3-x}O_4$ samples was further performed to study the cation distributions in the crystal structure using the GSAS EXPGUI computer program.[55] The goodness of the refinement (χ^2) and the reliability parameters (wR_p and R_p) defined as the following equations were used to judge the accuracy of the profile fitting,

$$wR_p = \sqrt{\frac{\sum w_i(I_{io} - I_{ic})^2}{\sum w_i I_{io}^2}} \quad (1)$$

$$R_p = \frac{\sum |I_{ko} - I_{kx}|}{\sum I_{ko}} \quad (2)$$

$$x^2 = \frac{\sum W_i(I_{io} - I_{ic})^2}{N - P} \quad (3)$$

where I_{io} and I_{ic} are the observed and calculated intensities at the ith step; I_k is the intensity assigned to the kth Bragg reflection at the end of the refinement cycle; w_i is the weight factor; N and P are the data point numbers and parameters, respectively. The χ^2, wR_p, and R_p parameters are generally proposed to be the good global indicators for the refinement process.[56−58] Figure 2 shows the graphical results of the Rietveld refinement for the samples with a comparison of the observed with the calculated intensities, and the refinement parameters obtained using the least-squares method are listed in Table 2. The starting model employed in the refinement was a random cation distribution of Zn^{2+} and Fe^{3+} ions at tetrahedral (A) and octahedral (B) sites with Fe^{2+} ions fixed at octahedral sites. Site occupancies of Zn and Fe were constrained to keep the stoichiometric ratio in the $Zn_xFe_{3-x}O_4$ samples. It can be learned from the results listed in Table 2 that the Zn^{2+} ions only occupy the A-site with x varying from 0.0 to 0.4, and when x > 0.4, the A-site is saturated and the Zn^{2+} ions turn to occupy B-site.

The morphologies and distributions of the $Zn_xFe_{3-x}O_4$ samples obtained from TEM are presented in Figure 3. As can be seen from the TEM images that all the samples behave as spherical shape nanoclusters assembled with smaller nanoparticles. For taking a close glimpse at the size distributions, we measured the sizes of 100 nanoclusters and nanoparticles selected from different observed images. The size distributions are displayed in the histograms as illustrated in Figures 3 and 4. It can be found that the samples' sizes obey a Gaussian distribution, which is in good agreement with the work reported in the early established publications.[20,34−36,59,60] The average diameters of the nanoparticles are listed in Table 1, and it can be seen that the evaluated average sizes of the nanoparticles are comparable with those obtained from the XRD measurement. Additionally, it can be learned from the TEM images that the average diameters of the nanoclusters decrease with x increasing from 0.0 to 0.4, behave with a constant size when x = 0.4 and 0.5, and then inversely increase with x increasing from 0.5 to 0.8. As for the nanoparticles, their average sizes decrease with x increasing from 0.0 to 0.5, and roughly remained a constant value from 0.5 to 0.8. This result suggests that the inversions of the doped Zn in the Fe_3O_4 lattice may play a crucial role in the morphologies and size distributions of the $Zn_xFe_{3-x}O_4$ samples, which is likely to result in a significant effect on their structural, magnetic, and thermodynamic properties.

3.2. Mössbauer Spectrum. To further study the effect of doped Zn on the structure, we have performed a Mössbauer spectra measurement on these nanoparticles. The zero-field ^{57}Fe Mössbauer spectra recorded at room temperature are shown in Figure 5 for the $Zn_xFe_{3-x}O_4$ with (x = 0.1, 0.2, 0.3, 0.4, 0.5, 0.8, and 1.0). The computed hyperfine parameters are listed in Table 3. It can be found that the spectra exhibit a superposition of two Zeeman sextets for (x < 0.5). The outer sextet corresponding to a higher magnetic field (H_A) is attributed to Fe^{3+} at A-site, and the inner sextet corresponding to lower magnetic field (H_B) is from Fe^{2+} and Fe^{3+} ions at B-site. The amount of Fe^{3+} presented at A- and B-sites can be estimated by determining the area under the Mössbauer absorption, and this estimation is in good agreement with the results from the XRD refinement. Also, it is obvious to see that the Fe relative amounts decrease continuously in the A-site from x = 0.1 to 0.4, confirming that the doping process leads to Fe^{3+} ions' movement from A-site to-B site. For x = 0.4, the area ratio of the iron ions at A-site and B-site is close to 3, which is almost the same ratio as the arrangement of $[Fe_{0.6}Zn_{0.4}]_A$-$[Fe_2]_BO_4$ presented in the XRD refinement. Moreover, the observed sextet is significantly broader with the higher level presence of Zn^{2+} ions, which gives rise to a variation in the coordination surroundings of the octahedral and tetrahedral sites. The different coordination surroundings consequently may enhance the distribution of hyperfine fields with broadened spectral lines. The decrease of the isomer shift (IS) with x varying from 0.1 to 1.0 illustrates that the Fe^{2+} amounts tend to decrease with the Zn^{2+} increasing in the samples. As for the magnetic hyperfine fields at A- and B-sites, they show a gradual monotonic decrease with the Zn^{2+} amounts increasing, which could result from the replacement of the nonmagnetic Zn^{2+} influencing the supertransferred hyperfine field at the central cation originating from the magnetic moments of the nearest-neighbor cations. Also, the replacement of Fe^{3+} ions with Zn^{2+} at A- and B-sites could make the inter-sublattice contribution decrease and conse-

DOI: 10.1021/acs.jpcc.5b10618
J. Phys. Chem. C 2016, 120, 1328−1341

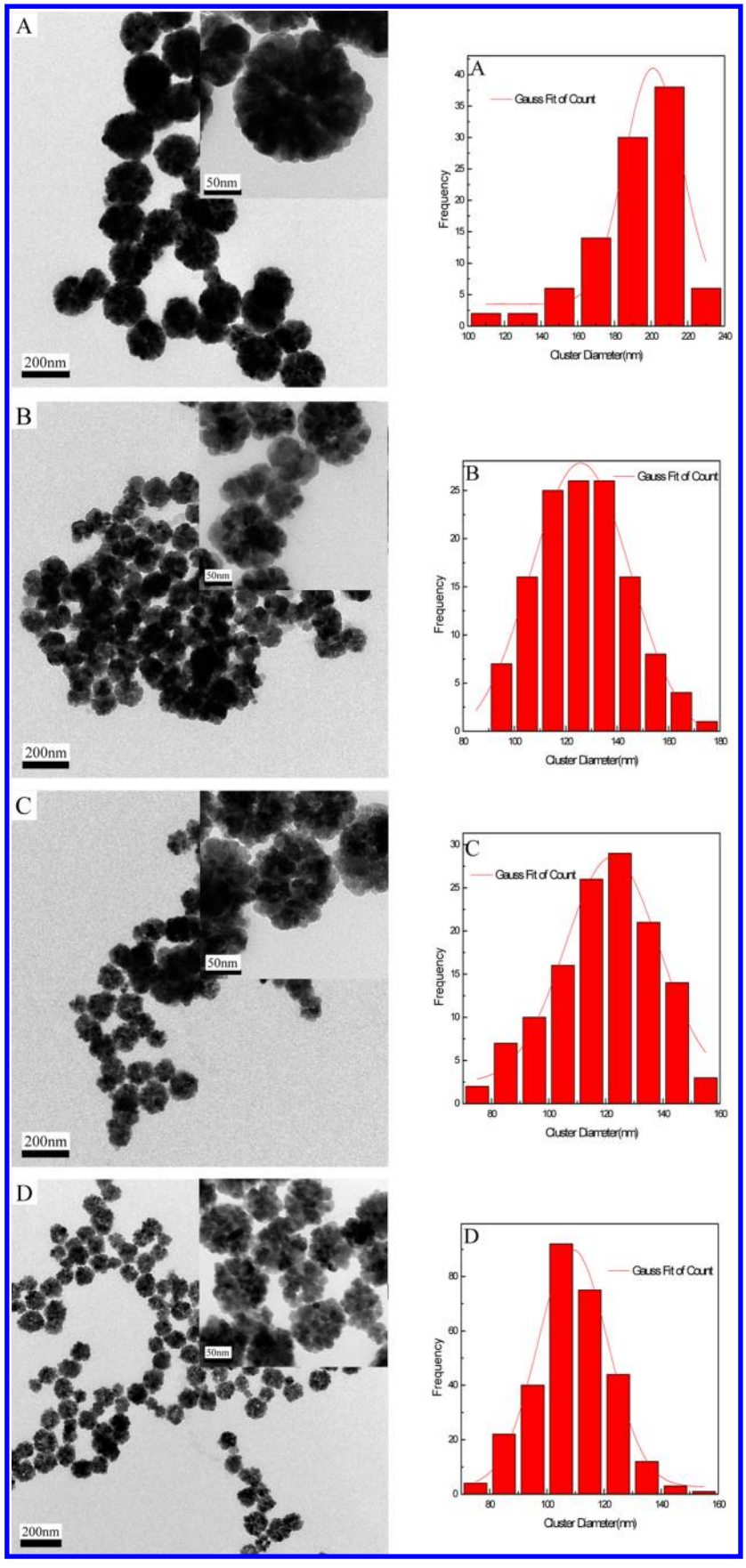

Figure 3. TEM images of $Zn_xFe_{3-x}O_4$ samples: (A) x = 0.0, (B) x = 0.1, (C) x = 0.2, (D) x = 0.3, (E) x = 0.4, (F) x = 0.5, and (G) x = 0.8.

DOI: 10.1021/acs.jpcc.5b10618
J. Phys. Chem. C 2016, 120, 1328−1341

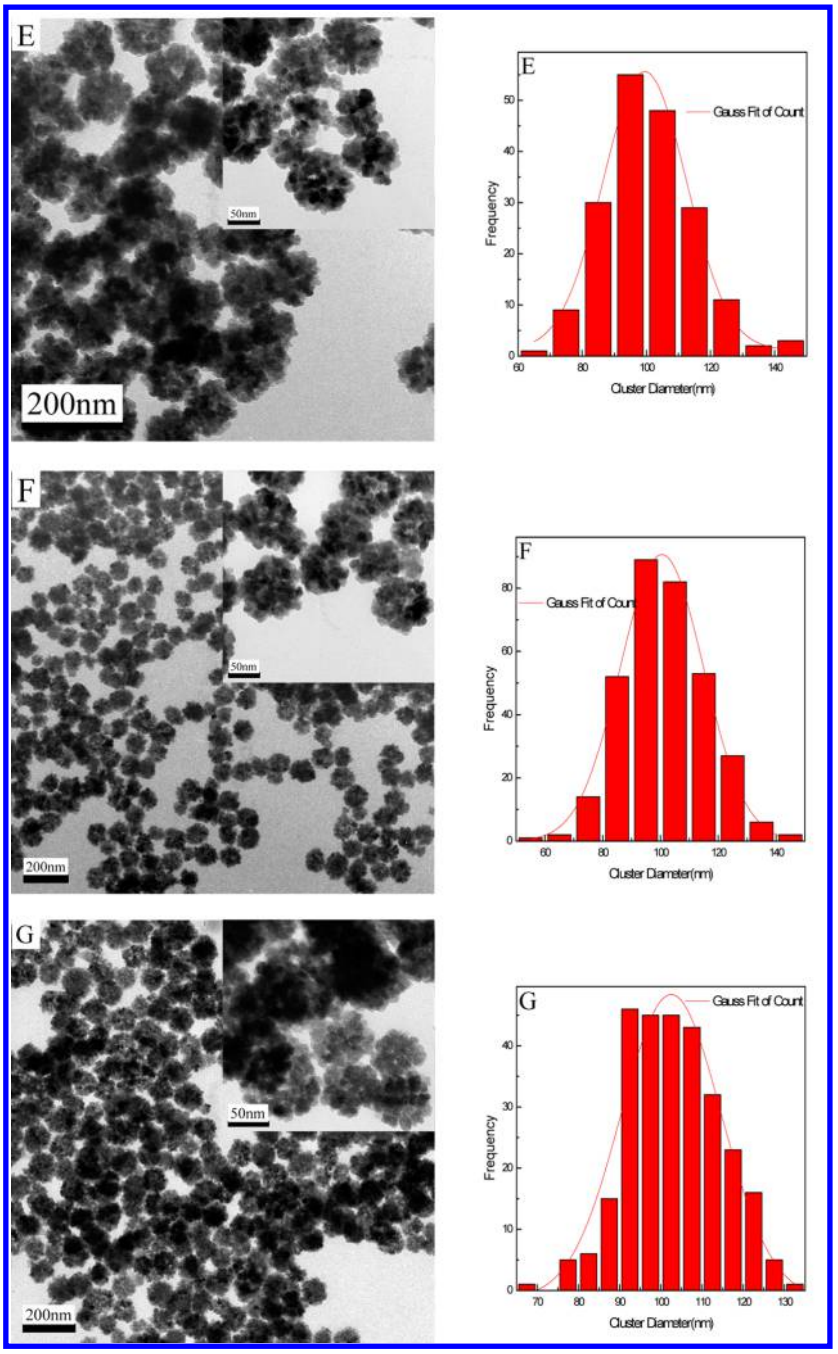

Figure 4. TEM images of $Zn_xFe_{3-x}O_4$ samples: (E) x = 0.4, (F) x = 0.5, and (G) x = 0.8.

quently reduce the ferromagnetic behavior and the magnetic coupling, i.e., decreasing H_A and H_B. This is also in good agreement with the magnetization results presented in the next section.

Moreover, for the sample with x = 0.5, the magnetic sextet presents much more broadened lines with a doublet appearing in the spectrum, suggesting that the nanoparticles with relatively small sizes may produce a slow relaxation phenomenon. In the case of x = 0.8, the spectrum exhibits a typical superparamagnetic behavior with a paramagnetic doublet superimposed on a broad component (magnetic relaxation spectrum). The doublet represents a paramagnetic response that indicates the magnetic hyperfine splitting of $Zn_xFe_{3-x}O_4$ has been collapsed, which is likely due to the thermally induced rapid reversals of the particle magnetic moments being faster than the nuclear larmor precession. Because of the distribution of energy barriers, some nanoparticles relax faster than the other particles at the given temperatures, consequently resulting in the broad ferromagnetic sextet and paramagnetic doublet appearing simultaneously. As for the sample with (x = 1.0), only one doublet was needed to fit the spectrum with the values of quadrupole splitting (QS) and IS being 0.49(2) mm/s and 0.35(2) mm/s, respectively. It is coincident with the previous reports that this IS value indicates a pure ferric state of iron in the sample, and the higher ΔQ value compared with the bulk ferrite could be assigned to the disordered Fe^{3+} environment caused by the nanoscales and the surface effects.[61]

3.3. Magnetization. The magnetization measurements were performed using the PPMS. Figure 6A shows the

DOI: 10.1021/acs.jpcc.5b10618
J. Phys. Chem. C 2016, 120, 1328−1341

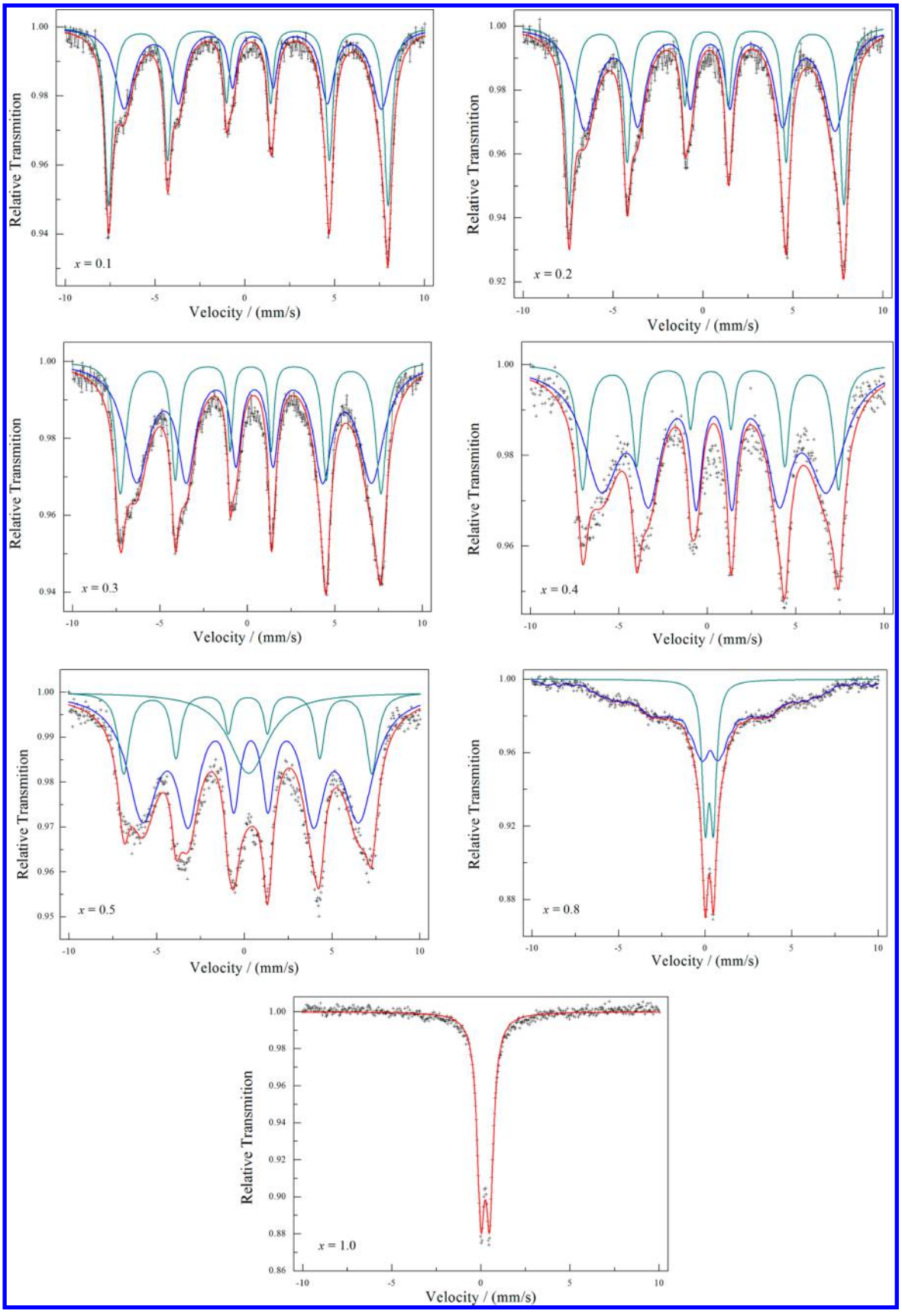

Figure 5. Mössbauer spectra of $Zn_xFe_{3-x}O_4$ samples with (x = 0.1, 0.2, 0.3, 0.4, 0.5, 0.8, 1.0) at room temperature.

hysteresis loops of the $Zn_xFe_{3-x}O_4$ samples with x = 0.0, 0.1, 0.2, 0.3, 0.4, 0.5, 0.8, and 1.0 at 300 K in an applied magnetic field from −10 to 10 kOe, and the corresponding saturated magnetization (M_s) and coercivity (H_c) are plotted in Figure

DOI: 10.1021/acs.jpcc.5b10618
J. Phys. Chem. C 2016, 120, 1328−1341

Table 3. Mössbauer Parameters for $Zn_xFe_{3-x}O_4$ Samples[a]

x	IS (mm/s)	QS (mm/s)	H (T)	A_o (%)	Γ (mm s^{-1})	site
0.1	0.56	−0.01	44.4	52	0.57	B
	0.31	−0.02	48.3	48	0.46	A
0.2	0.50	−0.01	43.1	61	0.66	B
	0.30	−0.01	47.4	39	0.41	A
0.3	0.50	−0.01	41.7	68	0.72	B
	0.29	−0.01	46.2	32	0.35	A
0.4	0.48	0.01	39.5	76	0.80	B
	0.29	−0.01	44.9	24	0.47	A
0.5	0.47	−0.01	38.3	68	0.86	B
	0.30	0.00	43.8	17	0.51	A
	0.36	2.03		15	1.70	
0.8	0.40	0.02	24.1	75.	0.44	
	0.35	0.47		25	0.43	
1.0	0.35	0.49			0.51	A

[a]IS is isomer shift, QS is quadrupole shift (splitting), H is hyperfine magnetic field, Γ is line width, and A_o is relative area of each site.

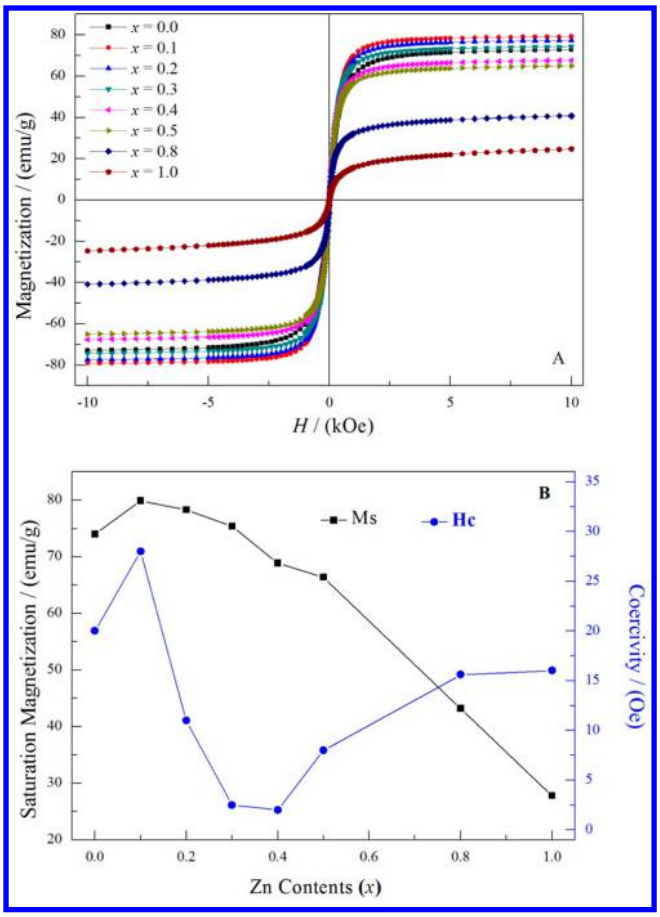

Figure 6. Results of magnetic hysteresis loops for $Zn_xFe_{3-x}O_4$ samples with (x = 0.0, 0.1, 0.2, 0.3, 0.4, 0.5, 0.8, and 1.0) at 300 K.

6B. The saturation magnetization was estimated by extrapolating the magnetization to high field regions using the following function[62]

$$M = M_s(1 - a/H) \quad (4)$$

where a is the fitting parameter. The magnetization is found to saturate up to the field of 10 kOe. This result indicates that all the samples show soft ferromagnetic behavior close to superparamagnetism when the particle size is decreased at room temperature. As can be seen from Figure 6B, the M_s value of Fe_3O_4 (x = 0) is about 75 emu/g, which is larger than the reported value of the sample prepared using a chemical coprecipitated technique.[34] For the other samples, the M_s is enhanced initially with the x increasing from 0.1 to 0.3 compared to the Fe_3O_4, and then reduced gradually with x from 0.4 to 1.0. This can be explained by considering the preferred occupation of A site for Zn cations.[63] According to Neel's two sublattices ferrimagnetism model,[64] the A and B sublattices are antiferromagnetically coupled, and the nonmagnetic Zn^{2+} ions would prefer to occupy the A-site. Therefore, a decrease of occupation fraction of Fe^{3+} at the A-site would reduce the magnetic moment of A-site and consequently increase the net magnetization. When x is larger than 0.4, the excess Zn^{2+} ions tend to partly substitute iron ions at B-sites, and the antiferromagnetic B−B direct interactions start flipping those B-site Fe^{3+} moments that are farthest from an A-site moment. This could result in a departure of the spin from colinearity.[65] In this case, the substitution with more Zn content could reduce the magnetic moment of B-sites and consequently result in a gradual decline of the net magnetic moment. However, when Zn contents increase from 0.1 to 0.3, the continuous decreasing of particle size may lead to a surface distortion and produce a magnetically dead layer at the surface, which could reduce the net magnetic moment in the nanoparticles and consequently make the sample with x = 0.1 possessing the largest saturated magnetization. As for the coercivity shown in Figure 6B, it can be seen that the H_c values of all the samples are smaller than 50 Oe at 300 K. This result is the same as those reported for other $Zn_xFe_{3-x}O_4$ with similar particle sizes.[34,66] It is also found that the variation of H_c shows a maximum value at the doped Zn content of 0.1, decreases with further increase of the doped Zn to 0.4, and then slightly starts to increase as x increasing from 0.4 to 1.0. The small increase of H_c in this x range is likely due to the growing sizes of the nanoclusters, which may result in a contribution of magneto-crystalline anisotropy in the materials.

Figure 7A−E shows the thermal magnetization curves measured in zero-field-cooled (ZFC) and field-cooled (FC) modes over the temperature range from 4 to 300 K for the $Zn_xFe_{3-x}O_4$ samples with x = 0, 0.2, 0.5, 0.8, and 1.0. The susceptibility of these $Zn_xFe_{3-x}O_4$ samples increases with the Zn doped into the lattice at first, and then appears to decrease with further enhancement of the Zn contents. This is in line with the magnetization measurement results. Furthermore, the blocking temperature (T_B)[67] of these samples was estimated from the maxima of the ZFC curves, while the value of irreversibility temperature (T_{irr}) was obtained at the point where ZFC and FC curves starting to split. These results are listed in Table 4, where T_{irr} represents the blocking temperature of particles with the highest energy barrier and the T_B is giving the average value of the blocking temperatures of all the particles. The difference between T_B and T_{irr} corresponds to the width of the blocking temperature distributions, and it also gives information regarding the grains' size distributions in the samples. From the T_B and T_{irr} data, it can be seen that the widths of blocking temperature distributions are getting smaller with the doping Zn amounts increasing. This observation indicates that the size distribution of the $Zn_xFe_{3-x}O_4$ particles is becoming smaller with x increasing, which is in rough agreement with the size distributions obtained in the TEM images. In addition, the T_{irr} appears to decrease with the Zn contents increasing, suggesting

DOI: 10.1021/acs.jpcc.5b10618
J. Phys. Chem. C 2016, 120, 1328−1341

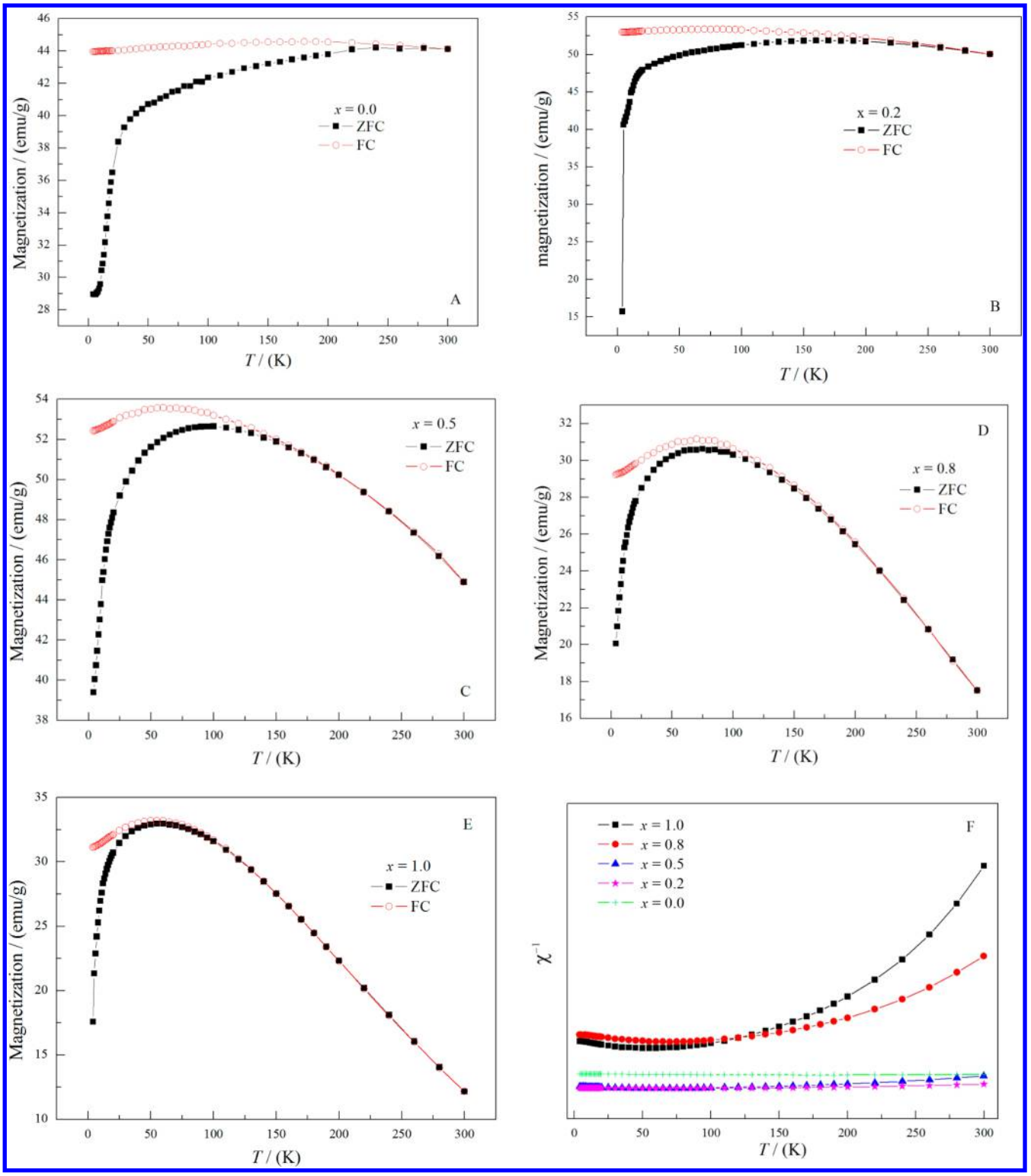

Figure 7. Zero-field-cooling (black ■) and field-cooling (red ○) curves of $Zn_xFe_{3-x}O_4$ samples: (A) x = 0, (B) x = 0.2, (C) x = 0.5, (D) x = 0.8, (E) x = 1.0, and (F) the inverse susceptibility χ^{-1} versus temperature.

that these nanostructured $Zn_xFe_{3-x}O_4$ turn to behave a paramagnetic property with further doping Zn in the materials.

The FC curves of the $Zn_xFe_{3-x}O_4$ samples with x = 0.0 and 0.2 in Figure 7A,B present a well-defined plateau in the entire experimental temperature region, suggesting that some dipolar interactions may exist among these nanoparticles.[68] In Figure 7C–E, the $Zn_xFe_{3-x}O_4$ with x from 0.3 to 1.0 exhibits a maximum in the FC curve at low temperatures, which may be associated with a transition from a paramagnetic state to antiferromagnetic state at the Neel temperature (T_N). Also, it can be seen that the FC magnetization decreases sharply below T_N, suggesting that the antiferromagnetic interaction becomes stronger at low temperatures. The Neel temperature presented in Table 3 is descending with the doping Zn increasing, which

DOI: 10.1021/acs.jpcc.5b10618
J. Phys. Chem. C 2016, 120, 1328–1341

Table 4. Summary of Magnetic Parameters for the $Zn_xFe_{3-x}O_4$ Samples[a]

x	M_s/(emu/g)	H_c/Oe	T_B/K	T_{irr}/K	T_N/K
0.0	74	20	>300	>300	
0.2	78	11	170	260	
0.5	66	8	100	170	60
0.8	43	16	80	180	60
1.0	28	16	60	110	55

[a] M_s is the saturated magnetization, H_c is the coercivity, T_B is the blocking temperature, T_{irr} is the irreversibility temperature, and T_N is the Neel temperature.

is likely caused by the decrease of A−B interaction as the A-site was gradually occupied by Zn, and consequently, the B−B interactions would dominant the magnetic properties. To further study this aspect, we calculated the inverse susceptibility of these samples and plotted it against the temperature in Figure 7F. It can be seen from this figure that the $\chi^{-1}(T)$ curve suggests a positive Curie−Weiss temperature (θ_{CW}) of about 150 K for the $ZnFe_2O_4$ sample when $\chi^{-1}(T)$ is extrapolated in the temperature range from 200 to 300 K. This positive value is quite lager than the reported bulk one (θ_{CW} = 50 K),[69] which may be associated with the enhancement of the exchange interaction between the sublattices.[70]

3.4. Heat Capacities. The thermodynamic property of these nanoparticles was studied by measuring the heat capacities of the samples with (x = 0, 0.2, 0.5, 0.8, and 1.0) using the PPMS in the temperature range from 1.9 to 300 K. As the metal oxides tend to absorb water in air,[71,72] we have performed thermogravimetry (TG) measurements on these samples to determine the water contents on the samples. On the basis of the TG results presented in Figure S1 and Table S1 (Supporting Information), the mole water contents represented in the sample molecular formula have been calculated to be $Fe_3O_4{\cdot}0.32H_2O$, $Zn_{0.2}Fe_{2.8}O_4{\cdot}0.69H_2O$, $Zn_{0.5}Fe_{2.5}O_4{\cdot}2.07H_2O$, $Zn_{0.8}Fe_{2.2}O_4{\cdot}2.45H_2O$, and $ZnFe_{2.0}O_4{\cdot}2.93H_2O$, respectively. The molar heat capacities of these samples were therefore calculated using these molecular formulas and plotted in Figure 8 and listed in Table S2. It can be seen from Figure 8 that the heat capacities of these samples increase with the doped Zn contents increasing from 0 to 1.0, except for the sample with x = 1.0 which has a smaller heat capacity than that of x = 0.8 in the temperature range roughly above 250 K. It is interesting to note that bulk $ZnFe_2O_4$ has a paramagnetic to antiferromagnetic transition around 10 K. However, as shown in the inset of Figure 8, this transition was not detected in our heat capacity curve, suggesting that the magnetic transition is likely spread out over a large temperature interval due to the sample's small particle sizes.[72,73]

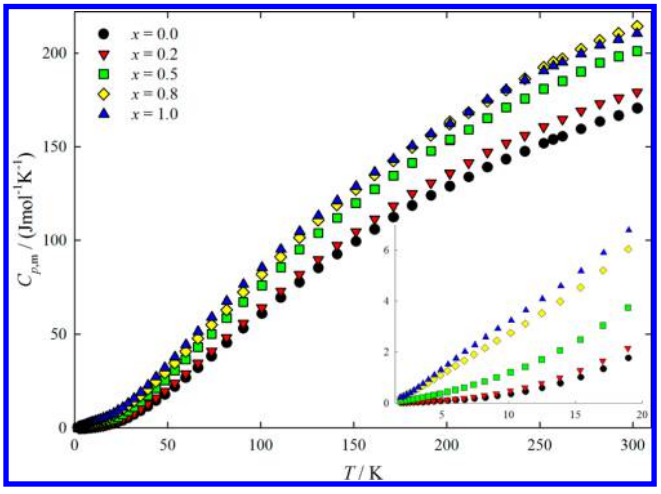

Figure 8. Heat capacity of $Zn_xFe_{3-x}O_4$ samples with (x = 0.0, 0.2, 0.5, 0.8, and 1.0) in the temperature range from 1.9 to 300 K.

The heat capacity of a substance at low temperatures can be expressed as a sum of contributions closely related to lattice vibrations, electrons, magnetons, nuclei, and impurities, and each property can be independently described using a proper theoretical model. Extracting these contributions by fitting the heat capacity data to theoretical models may provide important information about the physical property of a material.[50] To further investigate these physical properties, the heat capacities of these samples below 10 K were fitted to the following model

$$C_{p,m}/K = \gamma T + B_3T^3 + B_5T^5 + B_{fsw}T^{3/2}e^{-\Delta/T} + B_{asw}T^3e^{-\Delta/T} \quad (5)$$

where the γT term describes the contributions from electrons or lattice defects or oxygen vacancies in the sample; the (B_3T^3 + B_5T^5) term of odd powers in temperature is the harmonic lattice model in terms of the lattice vibration contribution; the $B_{fsw}T^{3/2}e^{-\Delta/T}$ and the $B_{asw}T^3e^{-\Delta/T}$ terms represent the ferromagnetic and antiferromagnetic behavior in the heat capacity, respectively; and the exponential function of $e^{-\Delta/T}$ in the magnetic terms represents a gap of the spin-wave spectrum generated in an ordered magnet when anisotropy occurs.[74−76]

All the possible low temperature fits using these terms and the corresponding fitting deviations are provided in Table S3 and Figure S2, respectively. It can be clearly concluded that Fit-1 is the best fit with physical meanings to model these heat capacity data, indicating that the Zn-doped samples with x = (0.0 and 0.2) include a ferromagnetic contribution and the samples with x = (0.5, 0.8, and 1.0) possess a antiferromagnetic contribution. Using these fitting results, the magnetic behaviors of the $Zn_xFe_{3-x}O_4$ samples can be further understood on the basis of the evolution of these magnetic contributions. It can be learned from the fitting parameters listed in Table 5 that the $Zn_xFe_{3-x}O_4$ samples have a ferromagnetic order as the doped Zn contents vary from 0 to 0.2, while the property turns out to be antiferromagnetic with the Zn contents from 0.5 to 1.0. This observation is identical to the results obtained in the above magnetic measurements. The sample with (x = 0.2) has a larger B_{fsw} term than that of the Fe_3O_4, suggesting that this Zn doping amount may enhance the ferromagnetic interaction in the sample. This is again in good agreement with the observations obtained in the magnetic measurements that the sample with x = 0.2 exhibits a larger magnetization than that of the sample with x = 0.0. Also, the antiferromagnetic contribution increases with x increasing from 0.5 to 1.0, which may be attributed to the gradual increase of the Zn content in the B-site which would enhance the antiferromagnetic interactions in the samples at low temperatures. Since the pure Fe_3O_4 and $ZnFe_2O_4$ possess well-known ferromagnetic and antiferromagnetic heat capacity contributions, respectively, it is reasonable to conclude that in these Zn-doped Fe_3O_4 samples the magnetic contribution is likely to change from ferromagnetic to antiferromagnetic with the Zn contents of x increasing from 0.2 to 0.5.

At temperatures above 70 K, the heat capacities were fitted to a combination of Debye and Einstein functions

DOI: 10.1021/acs.jpcc.5b10618
J. Phys. Chem. C 2016, 120, 1328−1341

Table 5. Fitting Parameters of Heat Capacities for the $Zn_xFe_{3-x}O_4$ Samples

param	x = 0.0	x = 0.2	x = 0.5	x = 0.8	x = 1.0
			Below 10 K		
γ/(mJ K^{-2} mol^{-1})	6.17	9.43	21.2	90.5	60.8
B_3/(mJ K^{-4} mol^{-1})	0.202	0.203	3.96	10.3	15.3
B_5/(mJ K^{-6} mol^{-1})			−0.0785	−0.224	−0.320
B_{fsw}/(mJ K$^{-5/2}$ mol^{-1})	3.20	9.01			
Δ_{fsw}/K	3.69	5.54			
B_{asw}/(mJ K^{-4} mol^{-1})			92.1	263	392
Δ_{asw}/K			29.4	29.4	30.1
Θ_D/K	424	443	187	139	126
RMS %	1.87	1.02	1.82	3.23	1.34
			From 10 to 70 K		
A_0/(J K^{-1} mol^{-1})	1.3004 × 10^{-03}	−3.7796 × 10^{-02}	−1.0704 × 10^{-01}	−4.4041 × 10^{-01}	−1.0588 × 10^{00}
A_1/(J K^{-2} mol^{-1})	3.1934 × 10^{-03}	2.3260 × 10^{-02}	6.7501 × 10^{-02}	2.7841 × 10^{-01}	5.3759 × 10^{-01}
A_2/(J K^{-3} mol^{-1})	1.8732 × 10^{-03}	−8.9141 × 10^{-04}	7.2316 × 10^{-03}	1.5138 × 10^{-02}	−1.0507 × 10^{-02}
A_3/(J K^{-4} mol^{-1})	1.9597 × 10^{-05}	4.5274 × 10^{-04}	−3.4878 × 10^{-04}	−2.2651 × 10^{-03}	−7.9497 × 10^{-04}
A_4/(J K^{-5} mol^{-1})	1.3263 × 10^{-05}	−1.3211 × 10^{-05}	3.0838 × 10^{-05}	1.5085 × 10^{-04}	1.0084 × 10^{-04}
A_5/(J K^{-6} mol^{-1})	−4.2675 × 10^{-07}	4.5026 × 10^{-07}	−8.3139 × 10^{-07}	−4.5595 × 10^{-06}	−3.4561 × 10^{-06}
A_6/(J K^{-7} mol^{-1})	5.0323 × 10^{-09}	−1.1047 × 10^{-08}	9.3912 × 10^{-09}	7.1930 × 10^{-08}	5.6661 × 10^{-08}
A_7/(J K^{-8} mol^{-1})	−2.1160 × 10^{-11}	1.3092 × 10^{-10}	−3.9064 × 10^{-11}	−5.7988 × 10^{-10}	−4.6196 × 10^{-10}
A_8/(J K^{-9} mol^{-1})		−5.7721 × 10^{-13}		1.8898 × 10^{-12}	1.5069 × 10^{-12}
RMS %	0.238	0.198	0.180	0.162	0.190
			Above 70 K		
n_D/mol	2.96	3.31	3.48	3.28	3.57
Θ_D/K	356	399	394	422	430
n_E/mol	3.13	2.97	2.61	1.90	3.15
Θ_E/K	599	677	691	721	962
A_1/(J K^{-2} mol^{-1})	9.5250 × 10^{-02}	1.8691 × 10^{-01}	2.9565 × 10^{-01}	4.3669 × 10^{-01}	5.0663 × 10^{-01}
A_2/(J K^{-3} mol^{-1})	1.6804 × 10^{-04}	−2.5399 × 10^{-05}	−1.0938 × 10^{-04}	−2.3483 × 10^{-04}	−6.4357 × 10^{-04}
RMS %	0.183	0.300	0.324	0.437	0.412

$$C_{p,m}/K = n_D D(\Theta_D) + n_E E(\Theta_E) + A_1 T + A_2 T^2 \quad (6)$$

where $D(\Theta_D)$ and $E(\Theta_E)$ are Debye and Einstein functions, and Θ_D and Θ_E are Debye and Einstein temperatures, respectively. n_D, n_E, A_1, and A_2 are adjustable parameters, and the sum of n_D and n_E is approximately the number of atoms in the molecule. The $(A_1T + A_2T^2)$ term represents an estimate for the difference between C_p and C_v.[73] As for the middle temperature range from 10 to 70 K, the heat capacities were fitted to a polynomial function. All the parameters from the above fitting models are listed in Table 5. Using these fits, we calculated the standard molar thermodynamic functions for the $Zn_xFe_{3-x}O_4$ samples with (x = 0, 0.2, 0.5, 0.8, and 1.0), and the standard molar entropies at 298.15 K and 0.1 MPa were determined to be (157.74 ± 1.58) J K^{-1} mol^{-1}, (167.63 ± 1.68) J K^{-1} mol^{-1}, (196.31 ± 1.96) J K^{-1} mol^{-1}, (214.29 ± 2.14) J K^{-1} mol^{-1}, and (219.94 ± 2.20) J K^{-1} mol^{-1}, respectively.

4. CONCLUSION

In summary, we have successfully demonstrated the novel synthesis of Zn-doped Fe_3O_4 nanoparticles using a facile one-step solvothermal method, and shown that the doping amounts could be accurately controlled in forming a stable Fe_3O_4 crystal structure. The XRD refinement and Mössbauer spectra investigation revealed that the doped Zn may occupy the tetrahedral A-site with x increasing from 0.0 to 0.4; then, the A-site is saturated, and the Zn turns to occupy B-site in the range x > 0.4. This inversion of the Zn occupation may play a crucial role in the evolutions of magnetic and thermodynamic properties of these Zn-doped Fe_3O_4 nanoparticles. The magnetic measurement at 300 K indicated that the saturated magnetizations of Zn-doped samples are initially enhanced with the x increasing from 0.1 to 0.3 compared to the Fe_3O_4 sample, and then reduced gradually with x from 0.4 to 1.0, due to the Zn occupation at A- and B-sites as well as the nanosize effect. The FC curve suggested that $Zn_xFe_{3-x}O_4$ with x from 0.3 to 1.0 is in an antiferromagnetic state at low temperatures. Additionally, the thermodynamic studies based on the heat capacity measurements have provided an interesting aspect that the magnetic heat capacity contribution at low temperatures could change from ferromagnetic to antiferromagnetic with Zn doping amounts increasing from x = 0.2 to 0.5. This suggests that the thermodynamic as well as the magnetic properties of Zn-doped Fe_3O_4 nanoparticles could be tunable by controlling the Zn doping amounts using the one-step solvothermal synthesis method developed in this work. We believe that this novel achievement obtained in the present study would provide a step forward for designing and synthesizing magnetic nanoparticles using the solvothermal process with underlying applications in the related fields.

■ ASSOCIATED CONTENT

Supporting Information

The Supporting Information is available free of charge on the ACS Publications website at DOI: 10.1021/acs.jpcc.5b10618.

Additional thermodynamic results (PDF)

DOI: 10.1021/acs.jpcc.5b10618
J. Phys. Chem. C 2016, 120, 1328−1341

AUTHOR INFORMATION

Corresponding Authors

*E-mail: shiquan@dicp.ac.cn. Phone and fax: +86-411-84379213.

*E-mail: zdnan@yzu.edu.cn. Phone and fax: +86-514-87959896.

Author Contributions

X.L., J.L., and S.Z. contributed equally.

Notes

The authors declare no competing financial interest.

ACKNOWLEDGMENTS

The authors gratefully acknowledge the financial support from the National Nature Science Foundation of China (21473198, 21273196, and 11205160) and the Priority Academic Program Development of Jiangsu Higher Education Institutions. Q.S. would like to thank Hundred-Talent Program founded by Chinese Academy of Sciences.

REFERENCES

(1) Kim, T. H.; Jang, E. Y.; Lee, N. J.; Choi, D. J.; Lee, K.-J.; Jang; Jung-tak; Choi; Jin-sil; Moon, S. H.; Cheon, Jinwoo. Nanoparticle Assemblies as Memristors. *Nano Lett.* **2009**, *9*, 2229−2233.

(2) Stone, R.; Willi, T.; Rosen, Y.; Mefford, O. T.; Alexis, F. Targeted Magnetic Hyperthermia. *Ther. Delivery* **2011**, *2*, 815−838.

(3) Lee, J. E.; Lee, N.; Kim, H.; Kim, J.; Choi, S. H.; Kim, J. H.; Kim, T.; Song, I. C.; Park, S. P.; Moon, W. K.; Hyeon, T. Uniform Mesoporous Dye-doped Silica Nanoparticles Decorated with Multiple Magnetite Nanocrystals for Simultaneous Enhanced Magnetic Resonance Imaging, Fluorescence Imaging, and Drug Delivery. *J. Am. Chem. Soc.* **2010**, *132*, 552−557.

(4) Shubayev, V. I.; Pisanic, T. R.; Jin, S. Magnetic Nanoparticles for Theragnostics. *Adv. Drug Delivery Rev.* **2009**, *61*, 467−477.

(5) Jordan, A.; Scholz, R.; Wust, P.; Schirra, H.; Schiestel, T.; Schmidt, H.; Felix, R. Endocytosis of Dextran and Silan-coated Magnetite Nanoparticles and the Effect of Intracellular Hyperthermia on Human Mammary Carcinoma Cells in Vitro. *J. Magn. Magn. Mater.* **1999**, *194*, 185−196.

(6) Fauconnier, N.; Bée, A.; Roger, J.; Pons, J. N. Synthesis of Aqueous Magnetic Liquids by Surface Complexation of Maghemite Nanoparticles. *J. Mol. Liq.* **1999**, *83*, 233−242.

(7) Zhang, Y.; Kohler, N.; Zhang, M. Surface Modification of Superparamagnetic Magnetite Nanoparticles and Their Intracellular Uptake. *Biomaterials* **2002**, *23*, 1553−1561.

(8) Doaga, A.; Cojocariu, A. M.; Amin, W.; Heib, F.; Bender, P.; Hempelmann, R. Synthesis and Characterizations of Manganese Ferrites for Hyperthermia Applications. *Mater. Chem. Phys.* **2013**, *143*, 305−310.

(9) Laurent, S.; Forge, D.; Port, M.; Roch, A.; Robic, C.; Vander Elst, L.; Muller, R. N. Magnetic Iron Ooxide Nanoparticles: Synthesis, Stabilization, Vectorization, Physicochemical Characterizations, and Biological Applications. *Chem. Rev.* **2008**, *108*, 2064−2110.

(10) Yan, S.; Tang, J.; Liu, P.; Gao, Q.; Hong, G.; Zhen, L. The Influence of Hollow Structure on the Magnetic Characteristics for Fe_3O_4 Submicron Spheres. *J. Appl. Phys.* **2011**, *109*, 07B535.

(11) Ito, A.; Shinkai, M.; Honda, H.; Kobayashi, T. Medical Application of Functionalized Magnetic Nanoparticles. *J. Biosci. Bioeng.* **2005**, *100*, 1−11.

(12) Parekh, K.; Upadhyay, R. V. Investigation of Dynamic Mmagnetic Properties of Surfactant Coated Monodispersed Fe_3O_4 Nanomagnetic Particles. *J. Nanofluids* **2012**, *1*, 93−96.

(13) Li, L.; Yang, Y.; Ding, J.; Xue, J. Synthesis of Magnetite Nanooctahedra and Their Magnetic Field-induced Two-/three-dimensional Superstructure. *Chem. Mater.* **2010**, *22*, 3183−3191.

(14) Roca, A. G.; Niznansky, D.; Poltierova-Vejpravova, J.; Bittova, B.; Gonzalez-Fernandez, M. A.; Serna, C. J.; Morales, M. P. Magnetite Nanoparticles with no Surface Spin Canting. *J. Appl. Phys.* **2009**, *105*, 114309.

(15) Li, L.; Li, G.; Smith, R. L.; Inomata, H. Microstructural Evolution and Magnetic Properties of $NiFe_2O_4$ Nanocrystals Dispersed in Amorphous Silica. *Chem. Mater.* **2000**, *12*, 3705−3714.

(16) Yao, C.; Zeng, Q.; Goya, G. F.; Torres, T.; Liu, J.; Wu, H.; Ge, M.; Zeng, Y.; Wang, Y.; Jiang, J. Z. $ZnFe_2O_4$ Nanocrystals: Synthesis and Magnetic Properties. *J. Phys. Chem. C* **2007**, *111*, 12274−12278.

(17) Mozaffari, M.; Manouchehri, S.; Yousefi, M. H.; Amighian, J. The Effect of Solution Temperature on Crystallite Size and Magnetic Properties of Zn Substituted Co Ferrite Nanoparticles. *J. Magn. Magn. Mater.* **2010**, *322*, 383−388.

(18) Jacintho, G. V. M; Brolo, A. G.; Corio, P.; Suarez, P. A. Z.; Rubim, J. C. Structural Investigation of MFe_2O_4 (M = Fe, Co) Magnetic Fluids. *J. Phys. Chem. C* **2009**, *113* (113), 7684−7691.

(19) Lu, Z. L.; Lv, L. Y.; Zhu, J. M.; Li, S. D.; Liu, X. C.; Zou, W. Q.; Zhang, F. M.; Du, Y. W. Magnetic and Transport Property Studies of Nanocrystalline $Zn_xFe_{3-x}O_4$. *Solid State Commun.* **2006**, *137*, 528−532.

(20) Pereira, C.; Pereira, A. M.; Fernandes, C.; Rocha, M.; Mendes, R.; Fernández- García, M. P.; Guedes, A.; Tavares, P. B.; Grenèche, J.; Araújo, J. P.; Freire, C. Superparamagnetic MFe_2O_4 (M = Fe, Co, Mn) Nanoparticles: Tuning the Particle Size and Magnetic Properties Through a Novel One-step Coprecipitation Route. *Chem. Mater.* **2012**, *24*, 1496−1504.

(21) George, M.; John, A. M.; Nair, S. S.; Joy, P. A.; Anantharaman, M. R. Finite Size Effects on the Structural and Magnetic Properties of Sol-gel Synthesized $NiFe_2O_4$ Powders. *J. Magn. Magn. Mater.* **2006**, *302*, 190−195.

(22) Mazario, E.; Morales, M. P.; Galindo, R.; Herrasti, P.; Menendez, N. Influence of the Temperature in the Electrochemical Synthesis of Cobalt Ferrites Nanoparticles. *J. Alloys Compd.* **2012**, *536*, S222−S225.

(23) Manova, E.; Kunev, B.; Paneva, D.; Mitov, I.; Petrov, L.; et al. Mechano-synthesis, Characterization, and Magnetic Properties of Nanoparticles of Cobalt Ferrite, $CoFe_2O_4$. *Chem. Mater.* **2004**, *16*, 5689−5696.

(24) Liu, C.; Rondinone, A. J.; Zhang, Z. J. Synthesis of Magnetic Spinel Ferrite $CoFe_2O_4$ Nanoparticles from Ferric Salt and Characterization of the Size-dependent Superparamagnetic Properties. *Pure Appl. Chem.* **2000**, *72*, 37−45.

(25) Hu, W.; Qin, N.; Wu, G.; Lin, Y.; Li, S.; Bao, D. Opportunity of Spinel Ferrite Materials in Nonvolatile Memory Device Applications Based on Their Resistive Switching Performances. *J. Am. Chem. Soc.* **2012**, *134*, 14658−14661.

(26) Tanaka, K.; Makita, M.; Shimizugawa, Y. Structure and High Magnetization of Rapidly Quenched Zinc Ferrite. *J. Phys. Chem. Solids* **1998**, *59*, 1611−1618.

(27) Nakashima, S.; Fujita, K.; Tanaka, K.; Hirao, K. High Magnetization and the High-temperature Superparamagnetic Transition with Intercluster Interaction in Disordered Zinc Ferrite Thin Film. *J. Phys.: Condens. Matter* **2005**, *17*, 137−149.

(28) Li, W.; Qiao, X.; Zheng, Q.; Zhang, T. One-step Synthesis of MFe_2O_4 (M = Fe, Co) Hollow Spheres by Template-free Solvothermal Method. *J. Alloys Compd.* **2011**, *509*, 6206−6211.

(29) Deng, H.; Li, X. L.; Peng, Q.; Wang, X.; Chen, J. P.; Li, Y. D. Monodisperse Magnetic Single-crystal Ferrite Nicrospheres. *Angew. Chem.* **2005**, *117*, 2842−2845.

(30) Guo, P.; Cui, L.; Wang, Y.; Lv, M.; Wang, B.; Zhao, X. S. Facile Synthesis of $ZnFe_2O_4$ Nanoparticles with Tunable Magnetic and Sensing Properties. *Langmuir* **2013**, *29*, 8997−9003.

(31) Li, Y. H.; An, S. Y.; Kim, C. S. Study of Site Occupancy in $Zn_xFe_{3-x}O_4$ Microspheres Based on Mössbauer Analysis. *IEEE Trans. Magn.* **2013**, *49*, 4287−4290.

(32) Yang, Z.; Li, Z.; Yang, Y.; Xu, Z. J. Optimization of $Zn_xFe_{3-x}O_4$ Hollow Spheres for Enhanced Microwave Attenuation. *ACS Appl. Mater. Interfaces* **2014**, *6*, 21911−21915.

(33) Liu, J.; Zhang, Y.; Nan, Z. Facile Synthesis of Stoichiometric Zinc Ferrite Nanocrystal Clusters with Superparamagnetism and High Magnetization. *Mater. Res. Bull.* **2014**, *60*, 270−278.

DOI: 10.1021/acs.jpcc.5b10618
J. Phys. Chem. C 2016, 120, 1328−1341

(34) Liu, J.; Bin, Y. Z.; Matsuo, M. Magnetic Behavior of Zn-doped Fe_3O_4 Nanoparticles Estimated in Terms of Crystal Domain Size. *J. Phys. Chem. C* **2012**, *116*, 134−143.
(35) Petrova, E.; Kotsikau, D.; Pankov, V. Structural Characterization and Magnetic Properties of Sol-gel Derived $Zn_xFe_{3-x}O_4$ Nanoparticles. *J. Magn. Magn. Mater.* **2015**, *378*, 429−435.
(36) Marand, Z. R.; Farimani, M. H. R.; Shahtahmasebi, N. Study of Magnetic and Structural and Optical Properties of Zn Doped Fe_3O_4 Nanoparticles Synthesized by Co-precipitation Method for Biomedical Application. *Nanomed. J.* **2014**, *1*, 238−247.
(37) Li, Y.; Li, Q.; Wen, M.; Zhang, Y.; Zhai, Y.; Xie, Z.; Xu, F.; Wei, S. Magnetic Properties and Local Structure Studies of Zn Doped Ferrites. *J. Electron Spectrosc. Relat. Phenom.* **2007**, *160*, 1−6.
(38) Cheng, Y. H.; Li, L. Y.; Wang, W. H.; Liu, H.; Ren, S. W.; Cui, X. Y.; Zheng, R. K. Tunable Electrical and Magnetic Properties of Half-metallic $Zn_xFe_{3-x}O_4$ from First Principles. *Phys. Chem. Chem. Phys.* **2011**, *13*, 21243−21247.
(39) Pati, S. S.; Philip, J. A Facile Approach to Enhance the High Temperature Stability of Magnetite Nanoparticles with Improved Magnetic Property. *J. Appl. Phys.* **2013**, *113*, 044314−044314.
(40) Wen, M.; Li, Q.; Li, Y. Magnetic, Electronic and Structural Properties of $Zn_xFe_{3-x}O_4$. *J. Electron Spectrosc. Relat. Phenom.* **2006**, *153*, 65−70.
(41) Sorescu, M.; Diamandescu, L.; Tarabasanu-Mihaila, D.; Teodorescu, V. Sequence of Phase in the Hydrothermal Synthesis of Zinc-doped Magnetite System. *Mater. Chem. Phys.* **2007**, *106*, 273−278.
(42) Zélis, P. M.; Pasquevich, G. A.; Stewart, S. J.; Fernández van Raap, M. B.; Aphesteguy, J.; Bruvera, I. J.; Laborde, C.; Pianciola, B.; Jacobo, S.; Sánchez, F. H. Structural and Magnetic Study of Zinc-doped Magnetite Nanoparticles and Ferrofluids for Hyperthermia Applications. *J. Phys. D: Appl. Phys.* **2013**, *46*, 125006−125006.
(43) Kozlowski, A.; Kakol, Z.; Zalecki, R.; Knight, K.; Sabol, J.; Honig, J. M. Powder Neutron Diffraction Studies of Zn-doped Magnetite. *J. Phys.: Condens. Matter* **1999**, *11*, 2749−2758.
(44) Hastings, J. M.; Corliss, L. M. An Antiferromagnetic Transition in Zinc Ferrite. *Phys. Rev.* **1956**, *102* (6), 1460−1463.
(45) Ehrhardt, H.; Campbell, S. J.; Hofmann, M. Magnetism of the Nanostructured Spinel Zinc Ferrite. *Scr. Mater.* **2003**, *48*, 1141−1146.
(46) Falk, B. G.; Pan, L.-S.; Evans, B. J.; Westrum, E. F., Jr. Low-temperature Phase Transitions of Fe_3O_4 with Innocuous Dopants. *J. Chem. Thermodyn.* **1979**, *11*, 367−378.
(47) Kozlowski, A.; Kakol, Z.; Zalecki, R.; Honig, J. M. Specific Heat of Low Doped Magnetite, $Fe_{3-x}Ti_xO_4$ and $Fe_{3-y}Zn_yO_4$. *J. Magn. Magn. Mater.* **1995**, *140−144*, 2083−2084.
(48) Aphesteguy, J. C.; Jacobo, S. E.; Lezama, L.; Kurlyandskaya, G. V.; Schegoleva, N. N. Microwave Resonant and Zero-field Absorption Study of Doped Magnetic Prepared by a Co-precipitation Method. *Molecules* **2014**, *19*, 8387−8401.
(49) Shi, Q.; Snow, C. L.; Boerio-Goates, J.; Woodfield, B. F. Accurate Heat Capacity Measurements on Powdered Samples Using a Quantum Design Physical Property Measurement System. *J. Chem. Thermodyn.* **2010**, *42*, 1107−1115.
(50) Gopal, E. S. R. *Specific Heats at Low Temperatures (International Cryogenics Monograph Series)*; Plenum Press: New York, 1966.
(51) Dai, R.; Zhang, S.; Yin, N.; Tan, Z.-C.; Shi, Q. Low-temperature Heat Capacity and Standard Thermodynamic Functions of *β*-D-(−)-arabinose ($C_5H_{10}O_5$). *J. Chem. Thermodyn.* **2016**, *92*, 60−65.
(52) Shi, Q.; Boerio-Goates, J.; Woodfield, B. F. An Improved Technique for Accurate Heat Capacity Measurements on Powdered Samples Using a Commercial Relaxation Calorimeter. *J. Chem. Thermodyn.* **2011**, *43*, 1263−1269.
(53) Rath, C.; Anand, S.; Das, R. P.; Sahu, K. K.; Kulkarni, S. D.; Date, S. K.; Mishra, N. C. Dependence on Cation Distribution of Particle Size, Lattice Parameter, and Magnetic Properties in Nanosize Mn−Zn Ferrite. *J. Appl. Phys.* **2002**, *91*, 2211−2215.
(54) Shannon, R. D. Revised Effective Ionic Radii and Systematic Studies of Interatomic Distances in Halides and Chalcogenides. *Acta Crystallogr., Sect. A: Cryst. Phys., Diffr., Theor. Gen. Crystallogr.* **1976**, *A32*, 751−767.
(55) Toby, B. H. EXPGUI, A Graphical User Interface for GSAS. *J. Appl. Crystallogr.* **2001**, *34*, 210−213.
(56) McCusker, L. B.; Von Dreele, R. B.; Cox, D. E.; Louer, D.; Scardi, P. Rietveld Refinement Guidelines. *J. Appl. Crystallogr.* **1999**, *32*, 36−50.
(57) Arana, M.; Galván, V.; Jacobo, S. E.; Bercoff, P. G. Cation Distribution and Magnetic Properties of LiMnZn Ferrites. *J. Alloys Compd.* **2013**, *568*, 5−10.
(58) Vucinic-Vasic, M.; Bozin, E. S.; Bessais, L.; Stojanovic, G.; Kozmidis-Luburic, U.; Abeykoon, M.; Jancar, B.; Meden, A.; Kremenovic, A.; Antic, B. Thermal Evolution of Cation Distribution/Crystallite Size and Their Correlation with the Magnetic State of Yb-Substituted Zinc Ferrite Nanoparticles. *J. Phys. Chem. C* **2013**, *117*, 12358−12365.
(59) Borisova, N. M.; Gorshenkov, M. V.; Koval, A. A.; Mozul, K. A.; Khovailo, V. V.; Shurinova, E. V. Structural and Magnetic Size Effects in Nanodisperse $Zn_xFe_{3-x}O_4$ Ferrite Systems. *Phys. Solid State* **2014**, *56* (7), 1334−1337.
(60) Surinwong, S.; Rujiwatra, A. Ultrasonic Cavitation Assisted Solvothermal Synthesis of Superparamagnetic Zinc Ferrite Nanoparticles. *Particuology* **2013**, *11*, 588−593.
(61) Pandey, B.; Litterst, F. J.; Baggio-Saitovitch, E. M. Preferential Spin Canting in Nanosize Zinc Ferrite. *J. Magn. Magn. Mater.* **2015**, *385*, 412−417.
(62) Singh, J. P.; Dixit, G.; Srivastava, R. C.; Agrawal, H. M.; Reddy, V. R.; Gupta, A. Observation of Bulk Like Magnetic Ordering Below the Blocking Temperature in Nanosized Zinc Ferrite. *J. Magn. Magn. Mater.* **2012**, *324*, 2553−2559.
(63) Smit, J.; Wijn, H. P. J. *Ferrites*; Wiley: New York, 1959.
(64) Neel, L. Proprietes Magnetiques des Ferrites-ferrimagnetism et Antiferromagnetisme. *Annales De Physique* **1948**, *3*, 137−198.
(65) O'Handley, R. C. *Modern Magnetic Materials: Principles and Applications*; Wiley: New York, 2000.
(66) Guo, X.; Zhu, H. J.; Si, M. S.; Jiang, C. J.; Xue, D. S.; Zhang, Z. H.; Li, Q. $ZnFe_2O_4$ Nanotubes: Microstructure and Magnetic Properties. *J. Phys. Chem. C* **2014**, *118*, 30145−30152.
(67) Denardin, J. C.; Brandl, A. L.; Knobel, M.; Panissod, P.; Pakhomov, A. B.; Liu, H.; Zhang, X. X. Thermoremanence and Zero-field-cooled/Field-cooled Magnetization Study of $Co_x(SiO2)_{1-x}$. *Phys. Rev. B: Condens. Matter Mater. Phys.* **2002**, *65*, 064422−064422.
(68) Pereira, A. M.; Pereira, C.; Silva, A. S.; Schmool, D. S.; Freire, C.; Grenèche, J.; Araújo, J. P. Unravelling the Effect of Interparticle Interactions and Surface Spin Canting in γ-Fe_2O_3@SiO_2 Superparamagnetic Nanoparticles. *J. Appl. Phys.* **2011**, *109*, 114319−114319.
(69) Yamada, Y.; Kamazawa, K.; Tsunoda, Y. Interspin Interactions in $ZnFe_2O_4$: Theoretical Analysis of Neutron Scattering Study. *Phys. Rev. B: Condens. Matter Mater. Phys.* **2002**, *66*, 064401−064401.
(70) Cullity, B. D.; Graham, C. D. *Introduction to Magnetic Materials*; Wiley: Hoboken, 2008.
(71) Boerio-goates, J.; Li, G.; Li, L.; Walker, T. F.; Parry, T.; Woodfield, B. F. Surface Water and the Origin of the Positive Excess Specific Heat for 7 nm Rutile and Anatase Nanoparticles. *Nano Lett.* **2006**, *6*, 750−754.
(72) Shi, Q.; Boerio-goates, J.; Woodfield, K.; Rytting, M.; Pulsipher, K.; Spencer, E. C.; Ross, N. L.; Navrotsky, A.; Woodfield, B. F. Heat Capacity Studies of Surface Water Confined on Cassiterite (SnO_2) Nanoparticles. *J. Phys. Chem. C* **2012**, *116*, 3910−3917.
(73) Zhang, Y.; Shi, Q.; Schliesser, J.; Woodfield, B. F.; Nan, Z. Magnetic and Thermodynamic Properties of Nanosized Zn Ferrite with Normal Spinel Structure Synthesized Using a Facile Method. *Inorg. Chem.* **2014**, *53*, 10463−10470.
(74) Shi, Q.; Zhang, L.; Schlesinger, M. E.; Boerio-Goates, J.; Woodfield, B. F. Low Temperature Heat Capacity Study of $Fe(PO_3)_3$ and $Fe_2P_2O_7$. *J. Chem. Thermodyn.* **2013**, *61*, 51−57.
(75) Shi, Q.; Zhang, L.; Schlesinger, M. E.; Boerio-Goates, J.; Woodfield, B. F. Low Temperature Heat Capacity Study of Fe_3PO_7 and $Fe_4(P_2O_7)_3$. *J. Chem. Thermodyn.* **2013**, *62*, 86−91.

DOI: 10.1021/acs.jpcc.5b10618
J. Phys. Chem. C 2016, 120, 1328−1341

(76) Shi, Q.; Zhang, L.; Schlesinger, M. E.; Boerio-Goates, J.; Woodfield, B. F. Low Temperature Heat Capacity Study of $FePO_4$ and $Fe_3(P_2O_7)_2$. *J. Chem. Thermodyn.* **2013**, *62*, 35−42.

DOI: 10.1021/acs.jpcc.5b10618
J. Phys. Chem. C 2016, 120, 1328−1341